Surface & Coatings Technology 476 (2024) 130199

Contents lists available at ScienceDirect

Surface & Coatings Technology

journal homepage: www.elsevier.com/locate/surfcoat

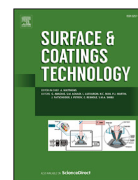

Full Length Article

Growth of Nb films on Cu for superconducting radio frequency cavities by direct current and high power impulse magnetron sputtering: A molecular dynamics and experimental study

M. Ghaemi [a,*], A. Lopez-Cazalilla [a], K. Sarakinos [b,c], G.J. Rosaz [d], C.P.A. Carlos [d], S. Leith [d], S. Calatroni [d], M. Himmerlich [d], F. Djurabekova [a]

[a] Helsinki Institute of Physics and Department of Physics, P.O. Box 43, FI-00014 University of Helsinki, Finland
[b] Department of Physics, P.O. Box 43, FI-00014 University of Helsinki, Finland
[c] KTH Royal Institute of Technology, Department of Physics, Roslagstullsbacken 21, 114 21 Stockholm, Sweden
[d] CERN, European Organization for Nuclear Research, 1211 Geneva, Switzerland

A R T I C L E I N F O

Keywords:
Nb thin film
Copper
Molecular dynamics
Magnetron sputtering deposition
Superconducting cavities of particle accelerators

A B S T R A C T

The use of superconducting radio frequency (rf) cavities in particle accelerators necessitates that copper (Cu) surfaces are coated by thin niobium (Nb) films, predominantly synthesized by magnetron sputtering. A key feature of the rf cavities is that they exhibit a complex three-dimensional geometry, such that during Nb film growth vapor is not deposited on a flat substrate. The latter, combined with the line-of-sight nature of the deposition flux in conventional magnetron sputtering methods (including direct current magnetron sputtering; DCMS) yields films with porous columnar morphologies on surfaces of the cavities that do not face the magnetron source. High-power impulse magnetron sputtering (HiPIMS) is a variant of sputtering that generates highly-ionized fluxes. Using electrical fields, such fluxes can be deflected to trajectories that are closer to the substrate normal and, thereby, dense and uniform layers can be deposited on all surfaces of the rf cavities. In the present work, we use classical molecular dynamics simulations to model Nb film growth on Cu substrates at conditions consistent with those prevailing during DCMS and HiPIMS. Our computational results are in qualitative agreement with experimental data (also generated in the present study), with respect to film morphology. Based on this agreement and by studying the evolution of the simulated systems, we suggest that the morphology of HiPIMS-grown films (as compared to their DCMS counterparts) is the result of the combined effects of deflection of ionized sputtered particles to trajectories parallel to the substrate normal, bombardment-induced interruption of crystal growth, and ballistic atomic rearrangement along with dynamic thermal annealing caused by energetic film-forming species. Moreover, the predictions of our model with respect to dynamic processes at the film-substrate interface and their effect on local epitaxial growth are discussed.

1. Introduction

Superconductive radio frequency (rf) cavities are key components in large-scale accelerators, including the SOLEIL synchrotron [1], HIE-ISOLDE [2,3], the Large Electron Positron (LEP) collider [4,5], and the Large Hadron Collider (LHC) [6]. The rf cavities are metallic chambers – originally made of bulk niobium (Nb) which is chosen due to its superior superconducting performance and stability at cryogenic temperatures [7] – that confine electromagnetic fields with the purpose of accelerating charged particles [8]. A low-cost alternative to bulk Nb is Nb-coated copper (Cu) [9], whereby depositing an Nb film (typical thickness 2 μm) on Cu rf cavities the advantages of both materials can be combined in a single platform. Using the Nb-Cu approach, the performance of the rf cavity crucially depends on the Nb-layer morphology and density, as well as on the film morphology and thickness uniformity on all cavity surfaces [10].

The rf cavities are complex-shaped curved objects on which Nb films are typically synthesized by direct current magnetron sputtering (DCMS) of a cylindrical Nb cathode that is assembled into the cavity [11,12]. DCMS is, in general, characterized by versatility and compatibility with large-scale substrates [13], yet it generates anisotropic fluxes, such that deposition predominantly occurs in the

* Corresponding author.
E-mail address: milad.ghaemikermani@helsinki.fi (M. Ghaemi).

https://doi.org/10.1016/j.surfcoat.2023.130199
Received 25 July 2023; Received in revised form 10 November 2023; Accepted 11 November 2023
Available online 20 November 2023
0257-8972/© 2023 The Author(s). Published by Elsevier B.V. This is an open access article under the CC BY license (http://creativecommons.org/licenses/by/4.0/).

line-of-sight [14,15]. Hence, growth of films with uniform thickness and morphology on all surfaces of substrates with complex three-dimensional geometries (including rf cavities) can be challenging. The reason is that material arrives on surfaces that do not face the magnetron source in off-normal directions, which is known to cause geometrical shadowing and porosity [16,17].

The above-described shortcomings associated with the line-of-sight nature of the sputter-deposition process can be mitigated by using a variant of magnetron sputtering termed high-power impulse magnetron sputtering (HiPIMS) [16–19]. In HiPIMS, power is applied to the sputtering cathode in the form of short (a few tens of μs long) unipolar pulses at duty cycles smaller than 10%. This operation mode allows the power density to reach values of a few KW cm^{-2}, leading to plasma densities about three orders of magnitude higher than those achieved in DCMS. The high plasma densities yield, in turn, up to 100% ionization for the sputtered material, in contrast to DCMS in which ionization degrees of only a few % are achieved [20,24]. The trajectories of the highly-ionized deposition fluxes can then be manipulated by electric fields (*e.g.*, by applying an electrostatic bias potential on the substrate), such that film-forming species can be deflected to near-to-normal incidence directions on surfaces that do not face the magnetron source. These deposition conditions have been shown experimentally to allow for deposition of uniform films on a wide range of complex substrates, including vias structures [16], metal cutting tools [17], and rf Cu cavities [12].

Despite having experimentally established that HiPIMS yields markedly different film morphologies, with respect to DCMS, on complex-shaped substrates, the exact atomistic mechanisms that govern these morphological differences are not fully understood. For instance, it is not clear to what extent growth is affected by the synergetic effect of trajectory modification and ballistic-induced atomic rearrangement due to bombardment of the growing surface by the energetic ionized species of the HiPIMS discharge. Moreover, local heating due to intense ion irradiation may also play a role in the film morphological evolution during HiPIMS. An atomistic picture of film growth can be provided by Molecular Dynamics (MD) simulations, which have been employed in the past decade for modeling film growth at conditions consistent with both DCMS and HiPIMS [21–23].

In the present work, we shed light on atomic-scale processes pertaining to the growth of Nb on Cu, by a combination of MD simulations and experiments. We deposit Nb coatings by DCMS and HiPIMS on Cu substrates that are oriented parallel to or titled with respect to the normal of the sputtering cathode. Morphological characterization of the deposited layers shows that HiPIMS yields a dense and uniform microstructure irrespective of substrate orientation. In contrast, DCMS yields a columnar morphology, while deposition on tilted substrates results in a porous microstructure in which the columns are tilted towards the direction of the deposition flux. Concurrently, we model the growth of Nb on Cu substrates by DCMS and HiPIMS. To resemble the plasma conditions and the plasma-surface interactions for both depositions methods, we systematically vary in our simulation model the atom energy and angle of incidence, as well as the substrate temperature during growth. For appropriate sets of the simulation parameters, our model reproduces qualitatively the key morphological features of DCMS- and HiPIMS-grown films seen in the experiments.

Based on the agreement between experimental data and simulations, and by carefully evaluating the evolution of the simulated systems, we suggest that the dense and uniform morphology of HiPIMS-deposited layers, as opposed to their DCMS counterparts, emanates from the combined effects of (i) deflection of ionized sputtered species to a direction parallel to the substrate normal; (ii) bombardment-induced interruption of crystal growth through all film formation stages; and (iii) ballistic-induced atomic rearrangement and local dynamic thermal annealing caused by the energetic HiPIMS species. We note that the ability of HiPIMS to yield dense films compared to DCMS, on both flat and complex-shaped three-dimensional substrates, is well-established in the literature. Our work provides a detailed atomic-scale picture of the processes that govern morphology differences between DCMS- and HiPIMS-grown films. In addition, our model predicts that intermixing may result in the presence of Cu not only in the vicinity of the film-substrate interface but also in the bulk of the film, as well as on the film surface, which is confirmed experimentally by detailed compositional analyses of the deposited layers. This process might be one of the reasons for performance deterioration in rf cavities. Hence, our study potential provides the scientific foundation for addressing a drawback in modern accelerator technologies. Moreover, our simulations show that Nb grows on Cu in an epitaxial manner with orientation relationships consistent with experimental data and models that are based on rigid lattice approximations. Concurrently, for simulation conditions consistent with HiPIMS, we find that the Nb lattice exhibits a tilt with respect to the substrate normal, which we explain on the basis of the mixed Nb-Cu layers formed at the film-substrate interface.

2. Research methodology

2.1. Computational methods

Molecular Dynamics (MD) is used to simulate growth of Nb on various surfaces of the Cu rf cavity (see Fig. 1) by DCMS and HiPIMS. The simulation box consists of an initial Cu FCC substrate (cell size ∼10.3 × 10.3 × 5.5 nm^3 containing ∼34 000 Cu atoms) the z-axis of which is oriented along one of the $\langle 1\,0\,0\rangle$, $\langle 1\,1\,1\rangle$, and $\langle 110\rangle$ directions. Thus deposition on the low-index crystallographic planes of the FCC structure – *i.e.*, (1 0 0), (1 1 1), and (1 1 0) – is modeled. Prior to commencing deposition of plasma and film-forming species, the substrate is relaxed at the simulation temperature T ($T = 300$, 450, 750, and 1000 K) using an NPT ensemble, zero pressure, and a Berendsen thermo and barostat for 60 ps (time constant $\tau = 0.3$ ps). Moreover, periodic boundary conditions (PBCs) are applied in all x-, y-, and z-axes of the simulation box. After the NPT relaxation step, PBCs along the z-axis are lifted and the bottom atomic layer is fixed to prevent transnational motion of the cell during particle deposition. This structure is again relaxed at the deposition temperature T for 10 ps, by applying a thermal bath (NVT ensemble) 5 Å above the fixed bottom layer and from the sidewalls for the cell, while the rest of the box is relaxed using an NVE ensemble. A schematic illustration of the initial configuration of the simulation cell is shown in Fig. 1(a).

Film growth is simulated by releasing particles 10 Å above the Cu surface, whereby this distance corresponds to roughly two times the cutoff distance of the interatomic potentials used to model the particle interactions in the system (details on the interatomic potentials are provided later in the present section). In a typical DCMS process, the ionization degree of the sputtered material (Nb in the present manuscript) is of the order of a few percent, while their energy exhibits a distribution with their most probable energy in the range 1-3 eV [24]. Ar^+ ions are also present in the DCMS discharge and impinge on electrically ground substrates (see experimental details in Section 2.2) with energies of the same order as the Nb atoms. Hence, for modeling growth at DCMS conditions, 25 000 Nb atoms with energies 1 eV/atom are deposited on the Cu substrate surface at $T = 450$ K, the latter being consistent with temperature used during experimental growth of Nb on Cu rf cavities [9,25]. Moreover, the effect of the orientation of the various surfaces of the rf cavity on growth is modeled by depositing Nb particles at various angles θ with respect to the substrate normal, *i.e.*, $\theta = 0°$, 45°, 65°, and 75°. We note that the effect of Ar^+ ions is not modeled since these species, considering their inert character and their rather low kinetic energy, are not expected to chemisorb on the surface, become incorporated in the growing layer, and cause considerable atomic displacement that will affect film morphological evolution.

In HiPIMS, ionization degrees of the sputtered material can reach up to 100% with energies of the order of a few tens of eV [20,24]. Moreover, in the HiPIMS growth experiment we model, a bias voltage

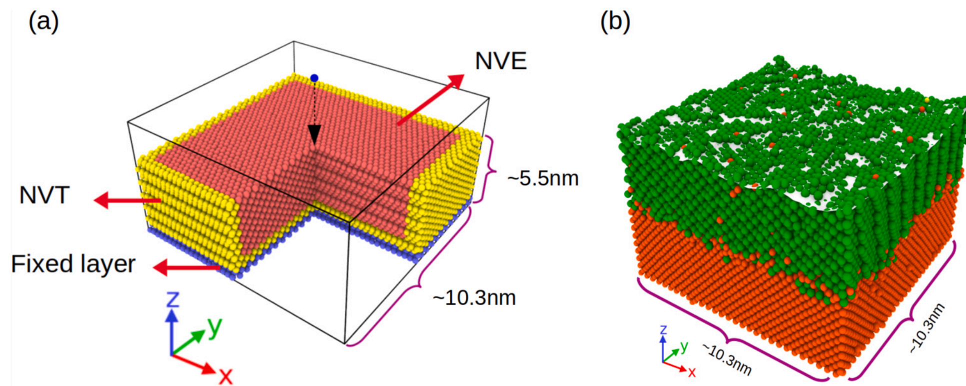

Fig. 1. (a) Schematic illustration of the simulation cell for the case of Cu(1 0 0) substrate, whereby blue, yellow, and red spheres indicate the atoms that belong to the fixed, NVT, and NVE layers, respectively. **(b)** Schematic illustration of the constructed surface mesh (white surface) after simulating deposition of 25 000 Nb and 5 000 Ar atoms on Cu(1 0 0) ($T = 300$ K) at conditions consistent with HiPIMS growth. The green and orange spheres represent the Nb and Cu atoms, respectively. In both panels **(a)** and **(b)**, the simulation cell dimensions along the x- and y-axis are provided.

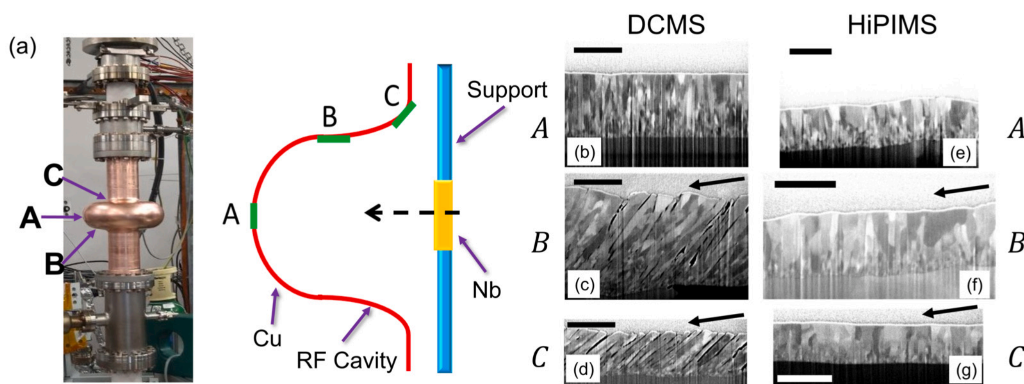

Fig. 2. (a) An example of the real cavity and a schematic illustration of the deposition geometry, representing the cylindrical sputtering cathode and the Cu stripe substrate. SEM analysis is performed on three different areas: one at the equatorial position of the cavity (area A), one on the flat slope of the cavity (area B), and one at the iris position (area C). These areas correspond to distinctly different orientations of the substrate surface relative to the Nb cathode normal (marked with a dashed arrow), such that vapor flux conditions ranging from near-to-normal (area A) to oblique-angle incidence (areas B and C) are probed. (b)-(g) Cross-sectional scanning electron micrographs of Nb films deposited on Cu substrates by DCMS (panels **(b)** - **(d)**) and HiPIMS (panels **(e)** - **(g)**) on areas A, B, and C, as indicated next to each panel. The scale bar corresponds to a length of 1 μm. The black arrows in panels (c), (d), (f), and (g) indicate the direction of the deposition flux.

of -75 eV is applied to the substrate, which results in acceleration of Nb^+ and Ar^+ ions in the substrate sheath region. Hence, ions arrive at the substrate with kinetic energies of the order of 100 eV. We simulate this experimental scenario by representing ions by the corresponding neutral species and deposit Nb (25 000 particles) and Ar atoms (5 000 particles) with energies of 100 eV/atom on the Cu substrate. This particle deployment scheme implicitly assumes that the Nb ionization degree is 100%, which enables us to probe the asymptotic-limit behavior during HiPIMS growth and better demonstrate its differences relative to DCMS growth. Every fifth Nb atom is followed by an Ar atom, which does not interact chemically with the substrate and has high probability to leave the surface after the impact. This Nb-to-Ar atom species ratio is based on experimental data on HiPIMS growth of Nb on Cu rf cavities [26]. Moreover, the deposition flux impinges on the substrate along the surface normal direction ($\theta = 0°$). Four different substrate temperatures ($T = 300$, 450, 750, and 1000 K) are simulated to explore potential effects of local heating on the film growth due to the intense ion irradiation during the HiPIMS process.

For normal incidence ($\theta = 0°$), particles are introduced into the simulation system every 0.6 ps. For all other angles θ used in DCMS growth simulations, and because of the relatively low particle energies (1 eV/atom), the time required for atoms to reach the surface is longer than for normal incidence. Hence, particles are released every 1.5 ps. Each newly introduced particle is always directed towards the center of the simulation cell surface, while the cell is randomly shifted across the periodic boundaries. This ensures that the impact site is random and far from the thermal bath at the boundaries [27,28]. To collect sufficient statistics, we perform five simulations for each combination of particle energy, incidence angle, and temperature, using different random number seeds. Structural information is recorded at an interval of 50 deposited particles.

Simulations are performed using the LAMMPS software package [29]. The Cu-Cu, Nb-Nb, and Cu-Nb interactions are, respectively, described by the force field models developed by Mishin [30], Ackland [31], and Zhang [32], within the same embedded atom method (EAM) formalism. These potentials have been successfully used to reproduce static bulk properties of the binary Nb-Cu system more accurately than other potentials. [33,34]. The close-range repulsive interactions between metal atoms are described by the Ziegler, Biersack, and Littmark (ZBL) universal potential, which is joined with the pair part of the EAM potential. For the interactions between Ar and Cu/Nb, we use the DMol potential [35]. The repulsive ZBL potential allows us to model the dissipation of the kinetic energy of the projectiles in the substrate via collision cascades, while the contribution of electronic excitations during the impact is taken into account as an additional friction force acting on energetic atoms in the material. Due to significant difference in ionic and electronic time scales, more accurate assessment of electron dynamics during the deposition process is not accessible within the atomistic approach which we choose in this study. However, as it was shown by Burgdorfer and Meye [36], possible potential energy effects related to the ionization state of the incoming ions during the ion irradiation of a metal surface are negligible, since the charge neutralization

Table 1
Coating parameters used in this study to elaborate the Nb/Cu films.

Deposition Parameter	DCMS	HiPIMS
Voltage (V)	375	590
Current (A)	3.47 (time-averaged)	344 (peak)
Pulsing Frequency (Hz)	-	100
Pulse Width (μs)	-	200
Pressure (Pa)	0.23	0.23
Deposition time (h)	1	1.5
Substrate bias potential (V)	0	-75

takes place very quickly within the first one or two atomic monolayers and does not modify notably the kinetic component of interactions.

Visualization of the simulation results and post-simulation analysis is performed using the OVITO freeware [37,38]. Post-simulation analysis includes determination of the atomic density of the film and construction of a surface mesh modifier (using the built-in OVITO function; see Fig. 1(b)), which is used to quantify the film root mean square roughness σ, computed as

$$\sigma = \sqrt{\frac{\sum_{i=1}^{N}(Z_i - \overline{Z})^2}{N}} \quad (1)$$

Z_i denotes the coordinate along the z-axis (*i.e.*, height) of the ith atom, $\overline{Z}$ is the mean height of all the atoms, and N is the number of atoms on the surface.

2.2. Experimental procedures

Films are deposited on oxygen-free electronic (OFE) grade Cu stripes (10 mm wide and 640 mm in length) that are bent using two stainless steel dyes to obtain a shape similar to the internal surface of a 704 MHz low beta cavity, as presented in a previous work [25]. The stripes are degreased using a commercial detergent, etched in a tri-acid mixture (H_2SO_4 42% vol, HNO_3 8% vol, HCl 0.2% vol), and passivated in a sulpho-chromic acid bath. Subsequently, they are rinsed with deionized water and ultra-pure alcohol, followed by dry-air blowing. The stripes are then mounted in the cavity and the coating setup is assembled in a cleanroom. The full coating apparatus and coating procedure description are available in [25]. Two different coatings are grown using a cylindrical cathode, one by Direct Current Magnetron Sputtering (DCMS) and another one by High Power Impulse Magnetron Sputtering (HiPIMS). For the HiPIMS deposition, a negative DC bias potential is applied on the substrate. A summary of the deposition parameters is given in Table 1. A schematic illustration of the deposition geometry is shown in Fig. 2(a).

After deposition, the Cu stripe is unfolded and the Nb film morphology is studied by cross-sectional scanning electron microscopy (SEM) using a Zeiss Sigma field emission gun instrument, equipped with an InLens detector (Secondary Electron), an Everhart-Thornley secondary electron detector, and a backscattered electron detector. Cross-sectional specimens are prepared using a ZEISS 'XB540' focused ion beam (FIB). For the cross-sectional milling, Pt deposition on top of the film is initially performed at a milling current of 300 pA and an accelerating voltage of 30 kV to deposit a 1 × 3 × 15 μm^3 protection barrier. Coarse milling at a current of 7 nA and accelerating voltage of 30 kV is then used to remove a 5 × 7 × 20 μm^3 region of material, before polishing the cross-sectional surface at a mild milling current of 300 pA. We note that the FIB cross-sections are cut perpendicularly to the longitudinal axis of the cavity to correlate the effect of the orientation of the cavity surface (with respect to the target normal) on film morphology. Three areas of the Cu stripe are investigated as shown in Fig. 2(a): one at the equatorial position of the cavity (area A), one on the flat slope of the cavity (area B), and one at the iris position (area C). These areas correspond to distinctly different orientations of the substrate surface with respect to the cathode surface normal (indicated with the dashed arrow), yielding vapor flux conditions that range from near-to-normal (A) to oblique-angle incidence (B and C).

The film composition is studied by X-ray photoelectron spectroscopy (XPS) depth-profiling using an ultra-high vacuum surface analysis system from Specs Surface Nano Analysis GmbH operating at a base pressure of $<2\times10^{-10}$ mbar. Al-Kα radiation is generated by an XR 50 M X-ray source in combination with a Focus 500 monochromator, while photonelectron spectra are sequentially acquired using a Phoibos 150 hemispherical electron analyzer equipped with nine channeltrons which installed in magic angle configuration with respect to the photon source. Depth compositional profiles are collected via sputter-etching the film surface by scanning a beam of 3 keV Ar^+ ions with a spot diameter of 0.8 mm across the surface in a square of 5×5 mm^2 using a differentially pumped IQE 12/38 ion source that creates an ion current of ~1 μA. At these operation conditions, the etching rate of a Ta_2O_5/Ta reference sample is 1.3 nm/min. The elemental composition was determined by considering the electron analyzer transmission function as well as fitting all spectra using CasaXPS version 2.3.24 and the algorithms implemented therein. For all spectra, a Shirley-type background correction was performed and the elemental sensitivity factors are based on the cross sections reported by Scofield [39] and considering an inelastic mean free path (IMFP) of the emitted electrons that is dependent on their kinetic energy: IMFP~$E_{\mathrm{kin}}^{0.7414}$ [40].

3. Results & discussion

3.1. Nb film morphology

Figs. 2 (b) through (g) present cross-sectional scanning electron micrographs of Nb films from the areas A, B, and C of the Cu stripe (see Fig. 2(a)), deposited by DCMS (panels (b) - (d)) and HiPIMS (panels (e) - (g)). For DCMS deposition on area A (Fig. 2(b); near-to-normal angle of incidence), the film exhibits a columnar and seemingly dense microstructure. Deposition on areas B and C (Fig. 2(c) and (d), respectively; oblique-angle deposition conditions) gives rise to intercolumnar porosity, while the columns are titled towards the general direction of the deposition flux (indicated by black arrows), as determined by the position of the sputtering cathode in relation to the substrate. HiPIMS, in contrast, yields similar film morphologies, irrespective of the area of deposition. Columns are still visible and no intercolumnar porosity is seen, *i.e.*, a compact and dense microstructure is obtained. Moreover, the column in-plane size is considerably larger than that of the columns seen in DCMS-grown films. The columnar morphology of the deposited layers is indicative of a polycrystalline microstructure, which is expected based on the fact that films are grown on a polycrystalline Cu substrate. The overall morphology evidenced in Fig. 2 is consistent with results obtained for deposition of metallic and ceramic films [16–18] on complex-shaped substrates by DCMS and HiPIMS.

Fig. 3 displays three-dimensional (3D) perspective snapshots of atomic assemblies generated at simulation conditions consistent with Nb film growth by DCMS. The snapshots are obtained after deposition of 25 000 Nb atoms on Cu(1 1 1) at a temperature $T = 1000$ K and an angle of incidence $\theta = 0°$, as well as for $T = 450$ K at $\theta = 0°$, 45°, 65°, and 75°. For all simulated conditions, the Nb films exhibit an $\langle 1\,1\,0 \rangle$ out-of-plane crystallographic orientation. For $T = 1000$ K and $\theta = 0°$ (Fig. 3(a)), the film microstructure consists of multiple grains separated by twin boundaries. In addition, the surface is uneven which means that roughness builds up at the film growth front. By evaluating data from five independent runs, we compute that the number of grains in the simulation box is $\bar{N}_{\mathrm{gr}} = 2.2 \pm 1.1$. Decrease of temperature to $T = 450$ K ($\theta = 0°$; Fig. 3(b)) still yields a multi-grain structure, but the number of grains increases to $\bar{N}_{\mathrm{gr}} = 3.6 \pm 1.5$. Furthermore, the film height increases, which indicates that the microstructure becomes less compact. More pronounced changes in film morphology are observed when changing the angle of incidence θ of the Nb atomic flux to the substrate

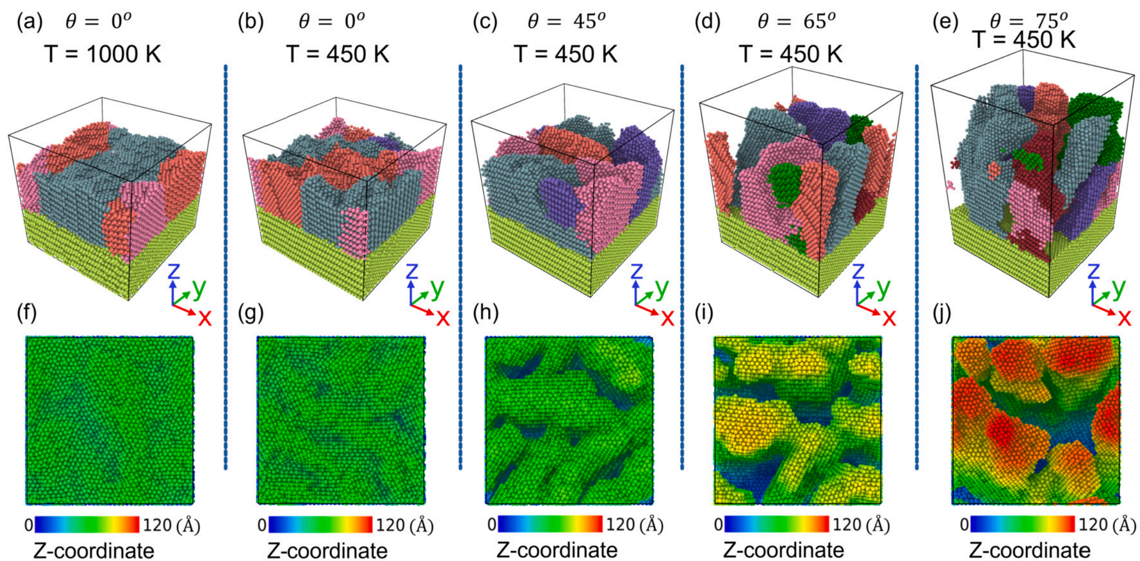

Fig. 3. Snapshots of atomic assemblies (atoms represented by spheres of different colors) generated at simulation conditions consistent with growth of Nb films by DCMS (deposition of 25 000 Nb atoms with an energy of 1 eV/atom) on Cu(1 1 1) surfaces at various temperatures T and incidence angles θ of the deposition flux, as indicated in each panel. The top row (panels **(a)** - **(e)**) presents three-dimensional perspective snapshots, while the bottom row (panels **(f)** - **(j)**) presents top-view snapshots. In panels **(a)** - **(e)** the colors represent different crystallographic grains, while in panels **(f)** - **(j)** the colors represent the Z-coordinate (*i.e.*, height) of the atoms, as indicated in the respective color scales.

(Figs. 3(c) to (e)). With increasing θ to 45°, 65°, and 75°, the number of grains in the simulation box increases to 4 ± 1.9, 5.8 ± 0.44, and 6.2 ± 1.3, respectively. Moreover, the grains (*i.e.*, columns) are tilted towards the direction of the incoming deposition flux (along the negative Y-coordinate), and the structure becomes seemingly more porous.

Further information with regards to the effect of simulation conditions on the film morphology is obtained by the top-view snapshots presented in Figs. 3(f) through (j). When Nb atoms are deposited at normal incidence ($\theta = 0°$), the film surface is relatively flat with a maximum peak-to-trough distance equal to 14.5 Å ($T = 1000$ K; Fig. 3(f)) and 17.3 Å ($T = 450$ K; Fig. 4(j)). Film height variations become more pronounced for off-normal deposition and the maximum peak-to-trough distances are 53.1, 81.3, and 101.6 Å for $\theta = 45°$, 65°, and 75°, respectively (Figs. 3(h) through (j)). Moreover, at conditions of off-normal deposition, the film surface is not continuous as parts of the Cu substrate surface remain exposed (more profoundly for $\theta = 65°$ and $\theta = 75°$).

Snapshots of simulations consistent with HiPIMS growth of Nb films on Cu(1 1 1) (25 000 Nb and Ar 5 000 atoms with energies of 100 eV/atom; $T = 300$, 450, 750, 1000 K; $\theta = 0°$) are presented in Fig. 4. The 3D perspective representations show that at $T = 300$ K (Fig. 4(a)) the film consists of two grains, while at all other temperatures (Figs. 4(b) through (d)) only one grain is observed. It should be, however, noted that a multi-grain morphology is not in general associated with the lowest simulated temperature, since simulated data for Nb film growth on Cu(1 0 0) and Cu(1 1 0) surfaces (see Figs. S1 and S2; supporting information file) show that the number of grains varies between one and three in a random fashion among the various simulated temperatures. The surface topography of the simulated assemblies is similar for all temperatures; the surface is rather flat with small height variations, while defects in the form of asperities are observed at the atomic scale. The top-view snapshots (Figs. 4(e) through (h)) better demonstrate the similarities of the surface topography, whereby the maximum peak-to-trough distance is 7 - 9 Å at all conditions. Moreover, by comparing the height variations in Fig. 4 with those of the top-view snapshots in Fig. 3 for $\theta = 0°$ (14.5 and 17.3 Å for $T = 1000$ and 450 K, respectively), it becomes evident that simulations at HiPIMS-like conditions result in flatter films with reference to simulations at DCMS-like conditions. Besides topography, crystallographic analysis of simulated Nb films in Figs. 4 and S1 and S2 show that they exhibit an ⟨1 1 0⟩ out-of-plane crystallographic orientation on Cu(1 1 1) and Cu(1 0 0), while they grow along the ⟨1 0 0⟩ direction on Cu(1 1 0). We also note that the same out-of-plane crystallographic orientations are obtained for simulations of DCMS Nb film growth on Cu(1 0 0) and Cu(1 1 0) surfaces (data not shown here).

To quantitatively assess the trends observed in Figs. 3 and 4, we compute the film atomic density N_{at} and surface roughness σ for all independent simulation runs. With respect to atomic density (data plotted as a function of the simulation conditions in Fig. 5(a)), we see that for simulation parameters consistent with the conditions prevailing during DCMS deposition (hollow circles; top and right axes) $N_{at} = 58.1 \pm 0.1$ nm^{-3} for $T = 450$ K and $\theta = 0°$. Increase of θ (at $T = 450$ K) causes N_{at} to decrease steeply and reach a value of 24.9 ± 1 nm^{-3} for $\theta = 75°$. It is also observed that an increase of the temperature to $T = 1000$ K for $\theta = 0°$ (hollow cross) does not significantly affect N_{at} which is equal to 57.6 ± 2.3 nm^{-3}. Simulation conditions that resemble HiPIMS growth (filled squares; bottom and left axes) yield an atomic density of 54.7 ± 1.2 nm^{-3} for $\theta = 0°$ and $T = 300$ K, which increases to 56.7 ± 0.4 nm^{-3} for $T = 450$ K, and effectively saturates for higher temperatures.

Surface roughness data are plotted in Fig. 5(b), for the same combination of simulation parameters as those in Fig. 5(a). The plot shows that simulations at DCMS-relevant conditions and for normal incidence of the deposition flux (hollow circles and cross; top and right axes) yield Nb films with $\sigma = 3.1 \pm 0.1$ and 2.8 ± 0.03 Å for $T = 450$ and 1000 K, respectively. An increase of the incident angle above $\theta = 0°$ ($T = 450$ K) leads to a larger surface roughness, such that $\sigma = 30.2 \pm 1$ Å for $\theta = 75°$. In contrast to DCMS conditions, simulations at HiPIMS-relevant conditions (filled squares; bottom and left axes) result in a σ that fluctuates between 1.1 and 1.3 Å for all temperatures. We also note that data for HiPIMS growth simulations on Cu(1 0 0) and Cu(1 1 0) (presented in Fig. S3 in the supporting information file) reveal the same trends as those evidenced in Fig. 5 for growth on Cu(1 1 1).

Formation of polycrystalline films commences with the nucleation of islands that exhibit random in-plane and out-of-plane crystallographic orientations. Further atom flux causes the islands to grow in size, until they interact with each other, merge, and eventually form clusters in which single-crystalline grains are separated by grain boundaries. This network of polycrystalline clusters is the template upon which the columnar microstructure develops, the latter being an inherent feature in physical vapor deposited (including magnetron-sputtered) polycrystalline layers [41–43]. In our simulations, Nb atoms are deposited on

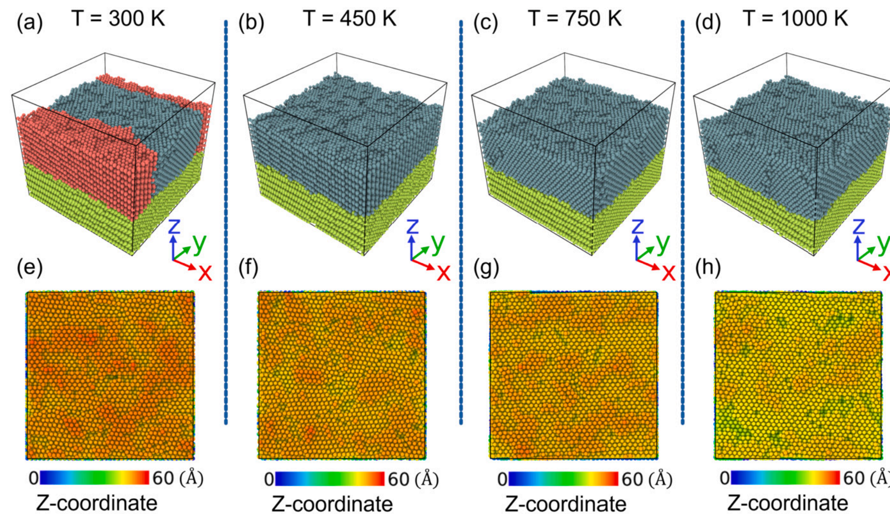

Fig. 4. Snapshots of atomic assemblies (atoms represented by spheres of different colors) generated at simulation conditions consistent with growth of Nb films by HiPIMS (deposition of 25 000 Nb and 5 000 Ar atoms with an energy of 100 eV/atom) on Cu(1 1 1) surfaces at an incidence of the deposition flux $\theta = 0°$ and various temperatures T, as indicated in each panel. The top row (panels **(a)** - **(d)**) presents three-dimensional perspective snapshots, while the bottom row (panels **(e)** - **(h)**) presents top-view snapshots. In panels **(a)** - **(d)** the colors represent different crystallographic grains, while in panels **(e)** - **(h)** the colors represent the Z-coordinate (*i.e.*, height) of the atoms, as indicated in the respective color scales.

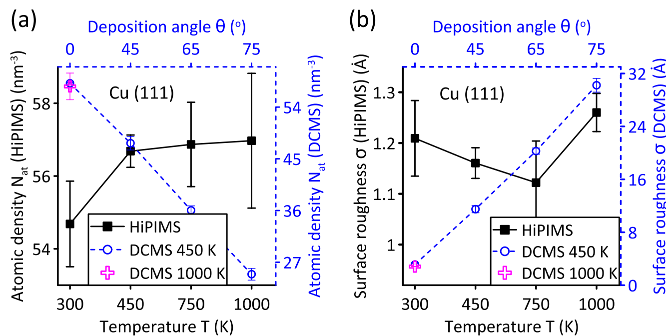

Fig. 5. Atomic density N_{at} (panel **(a)**) and surface roughness σ (panel **(b)**) of atomic assemblies generated at simulation conditions consistent with growth of Nb films on Cu(1 1 1) by DCMS and HiPIMS. In both panels the left-bottom axes plot data from simulations at HiPIMS-relevant parameters vs. temperature T, for deposition flux angle $\theta = 0°$ (filled squares), while the right-top axes plot data from simulations at DCMS-relevant parameters vs. deposition flux angle θ at $T = 450$ K (hollow circles) and $T = 1000$ K (hollow crosses). The solid and dashed lines are guides to the eye only.

single-crystalline Cu surfaces upon which epitaxial growth that yields a well-defined out-of-plane crystallographic orientation is expected. This notwithstanding, a multigrain columnar morphology is reproduced for simulation parameters resembling DCMS growth (Figs. 3(a) and (b)), as the film-substrate orientation relationship allows for crystalline Nb domains with different in-plane orientations to nucleate and grow (see Section 3.3 for more details on the epitaxial orientation relationships on the various Cu surfaces). Concurrently, atomic shadowing at off-normal deposition conditions (*e.g.*, on surfaces of the rf Cu cavity that do not face the sputtering source) exacerbate atomic shadowing, leading to faster growth rate and tilt of columns towards the incoming deposition flux, as well as to an underdense morphology [44], as seen in Figs. 2(c) and (d). The snapshots presented in Figs. 3(c) through (e), and the data plotted in Fig. 5 support this notion, which indicates that our simulation model describes the fundamental atomic-scale processes that govern morphological evolution of Nb films on the complex-shaped Cu rf cavities during typical DCMS conditions.

In contrast to DCMS, the HiPIMS discharge provides ample numbers of Nb^+ ions that can be deflected to trajectories parallel to the surface normal – and thereby mitigate effects of off-normal deposition on film morphology [16–19,45] – by applying an electrostatic bias potential to the substrate. Our model explicitly accounts for this effect by choosing $\theta = 0°$ for all simulation runs; which yield films in which the Nb grains grow perpendicularly to the substrate surface (Figs. 4(a) through (d) and Figs. S1 and S2), qualitative agreement with the experimental data in Figs. 2(e) through (g)).

The other feature of HiPIMS accounted for in our model is that ionized plasma species (both Nb^+ and Ar^+) are accelerated and impinge on the growing surface with energies of a few tens to hundreds eV, depending on the applied bias potential (100 eV/atom in our simulations). Energetic bombardment has been shown to affect morphological evolution by either increasing or decreasing nuclei density (relative to deposition without energetic bombardment), due to substrate cleaning [46], preferential sputtering [47], enhancement of adatom mobility [48], cluster dissociation [49], point-defect creation [50], adatom generation [51], and nucleation at ion-induced adatom clusters [52,53]. To explore the relevance of the above-mentioned mechanisms in our simulations, we present in Fig. 6 top-view and 3D perspective snapshots corresponding to the initial film growth stages up to a coverage of 1 monolayer (ML). We note here that 1 ML is the number density of Nb atoms required to form a complete (1 1 0) layer (1.3×10^{15} cm^{-2}). The top (panels (a) - (e)) and bottom (panels (f) - (j)) rows in Fig. 6 present data from simulations at conditions resembling DCMS and HiPIMS deposition, respectively, while all data are from simulations at $T = 450$ K and $\theta = 0°$.

The data corresponding to DCMS show the typical stages of film formation. Islands consisting of ~10-15 atoms nucleate (0.2 ML; panel (a)) and grow both in-plane and out-of-plane (0.45 ML; panel (b)). With continued deposition (0.75 ML; panel (c)) island impingement occurs and an interconnected network of elongated clusters is formed at 1 ML (panel (d)). Moreover, for coverage of 1 ML, the islands typically consist of 3 layers (also seen in the 3D perspective snapshot in panel (e)), and large parts of the Cu substrate remain uncovered (seen in both panel (e) and magnified section of panel (d)), *i.e.*, the film exhibits a 3D morphological evolution. The network of interconnected islands also features boundaries between different domains (marked with dashed lines in panel (d)), upon which the multigrain structure observed in Figs. 3(a) and (f)) is formed.

Snapshots for simulations at conditions resembling HiPIMS show that at 0.2 ML (panel (f)) the film surface features aggregates that contain a few Nb atoms only. These aggregates do not lead to well-defined Nb islands with continued deposition, but rather the number of Nb

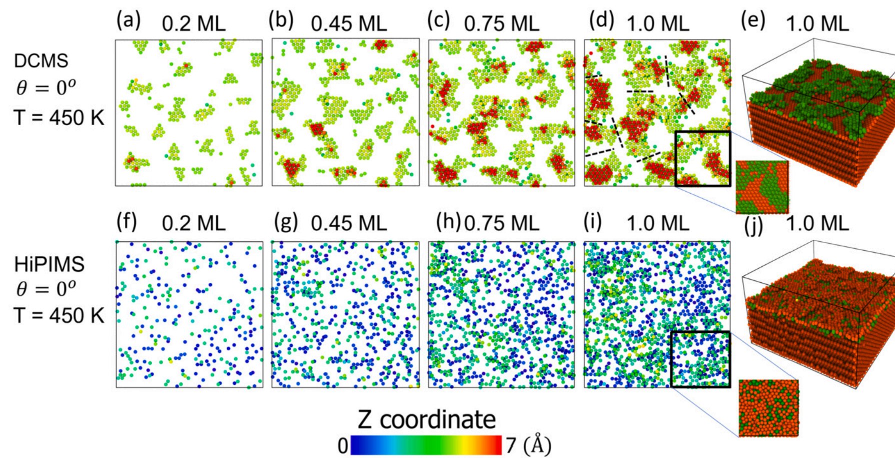

Fig. 6. Top-view and 3D perspective snapshots of atomic assemblies (atoms represented by spheres of different colors) generated at simulation conditions consistent with the growth of Nb films by DCMS (panels **(a)** - **(e)**; deposition of 25 000 Nb atoms with an energy of 1 eV/atom) and HiPIMS (panels **(f)** - **(j)**; deposition of 25 000 Nb and 5 000 Ar atoms with an energy of 100 eV/atom) on Cu(1 1 1) surfaces at a temperature $T = 450$ K and an incidence angle of the deposition flux $\theta = 0°$. The top-view snapshots (panels **(a)**, **(b)**, **(c)**, **(d)**, **(f)**, **(g)**, **(h)**, and **(i)**) present data at various coverages up to 1 monolayer (ML). The 3D perspective snapshots (panels **(e)** and **(j)**) show data at 1 ML coverage. One ML is the number density of Nb atoms required to form a complete (1 1 0) layer (1.3×10^{15} cm^{-2}). The Cu adatoms have been removed from the top-view snapshots for clarity, except for the magnified sections in panels (d) and (i).

adatom aggregates increases (0.45 ML; panel (g)), and eventually form an interconnected network of rather flat clusters (2 atomic layers; panels (h) and (i)). Moreover, considerable intermixing with substrate Cu atoms is observed (3D perspective snapshot in panel (j) and magnified section of panel (i)). This intermixing is the result of ballistic sputtering of the substrate by energetic Nb atoms and thermally-activated diffusion, as discussed in detail in Section 3.2. By comparing the top and bottom snapshot rows in Fig. 6, we conclude that energetic bombardment at simulation conditions relevant for HiPIMS growth leads to increased nucleation density via adatom cluster generation. These adatom clusters become embedded into Cu layers formed by out-diffusing substrate atoms, and lead to a few mixed Nb-Cu crystalline domains upon which the Nb layers consisting of one to three grains grow (Figs. 4, S1, and S2)). The suppression of columnar morphology in polycrystalline films has been attributed to ion-bombardment-induced interruption of local epitaxial growth (*i.e.*, crystal growth) on grain facets, that causes repeated nucleation and yields an equiaxed morphology [41–43,54]. The atomistic pathway suggested by our model is consistent with the notion of repeated nucleation (our simulations predict an increase in nucleation density). However additional mechanisms, including Nb and Cu intermixing at the film-substrate interface, may also be relevant for explaining the morphological evolution of Nb coatings deposited by HiPIMS on rf Cu cavities.

3.2. Dynamic processes at the Nb-Cu interface

In Section 3.1, we establish that our MD simulations qualitatively reproduce key features pertaining to growth morphology of Nb films deposited on Cu rf cavities by DCMS and HiPIMS. We then leverage the agreement between model and experiment to shed light on atomic-scale mechanisms that govern film morphological evolution. In the present Section, we use the experiment-consistent picture provided by our simulations as foundation for studying atomistic processes at the Nb-Cu interface that may be relevant for growth evolution and composition of Nb films.

The Nb^+ and Ar^+ ions in the HiPIMS deposition process are accelerated towards the substrate surface by a negative electrostatic bias of a few tens to hundreds of volts, resulting in energetic impacts on the surface of the substrate and the growing film. Although the energy of these impacts is too low for triggering substantial bulk atomic rearrangement, it can lead to sputtering of surface atoms, ultimately causing erosion and roughening of the substrate surface. This, in turn, may affect the substrate and film surface morphology and influence the final structure of the interface. To explore the relevance of such processes in our simulations, we plot in Figs. 7(a) through (d) Cu and Nb atomic concentration profiles (solid and dashed lines, respectively) along the z-axis of the cell box after the completion of the simulation. Data are presented in the form of atomic content ratio of Nb and Cu with respect to the total number of atoms in the simulated system. The vertical dashed lines mark the z coordinate of the Cu substrate surface prior to commencing the Nb and Ar particle deposition.

Fig. 7(a) presents data for DCMS deposition simulations on Cu(1 1 1), whereby the different line colors correspond to results of simulations at different deposition flux angles θ, as designated in the figure legend. The curves show for all deposition angles the position of the film-substrate interface – determined as the intersection of the Nb and Cu concentration profile lines – coincides with the position of the initial Cu substrate surface. Moreover, the region in which Cu and Nb are intermixed has a width of 20 Å.

Concentration profile data for HiPIMS deposition simulations on Cu(1 0 0), Cu(1 1 0), and Cu(1 1 1) are plotted in Figs. 7(b), (c), and (d), respectively. Different line colors are results from simulations at different deposition temperatures ($\theta = 0°$ for all simulations), as indicated in the figure legend. In contrast to the DCMS simulations, HiPIMS conditions result in an interface z position that is lower than that of the initial Cu surface, *i.e.*, the interface moves deeper into the bulk of the Cu substrate. This can be explained by the energetic (100 eV/atom) impact of Nb and Ar atoms that sputter-erode the substrate surface; a process that is not active during DCMS simulations in which the Nb atoms impinge on the substrate with energies of 1 eV/atom that are below the sputtering threshold. Concurrently, the width of the region across which Nb and Cu intermixing occurs is of the order of 20 Å, *i.e.*, similar to that for DCMS simulations. This indicates that intermixing is not a ballistic process, but it is rather mediated by the thermal inter-diffusion of the two species. This is further supported by the fact that the magnitude of intermixing increases with increasing temperature and reaches the maximum of $T = 1000$ K. We also see in Figs. 7(b) - (d) that, besides the film-substrate interface, there is a non-zero concentration of Cu through the Nb film, with the largest Cu content being in the vicinity of the film surface (marked with a black arrow), in particular for $T = 1000$ K. This feature is not seen in the DCMS deposition simulation data (Fig. 7(a)), which can be explained by the absence of intense mixing via collision cascades and atomic sputtering that can allow Cu atoms to propagate toward the top of the film and segregate at the growth front. Moreover,

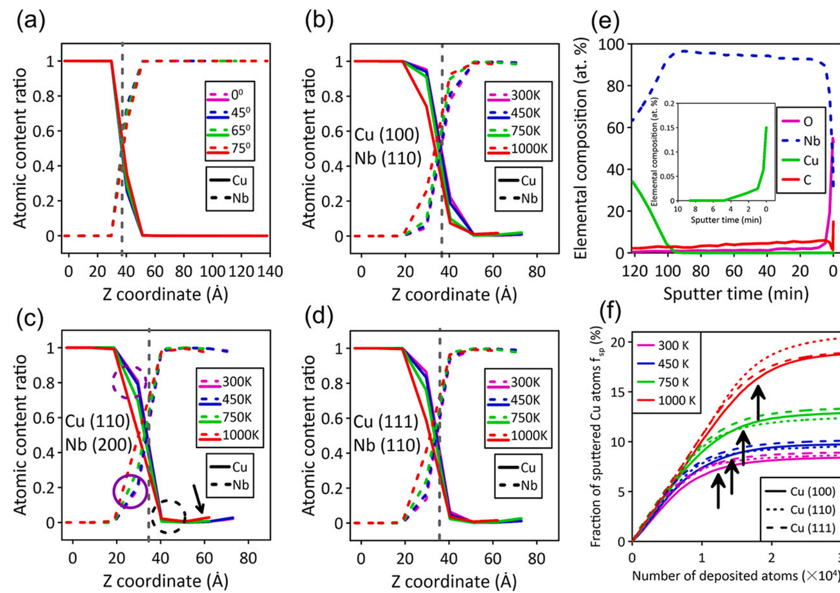

Fig. 7. (a) - (d) Cu and Nb atomic concentration profiles (solid and dashed lines, respectively) along the z-axis of the cell box after the completion of the simulation for DCMS (panel (a); Cu(1 1 1) substrates) and HiPIMS (panels (b), (c), and (d); Cu(1 0 0), Cu(1 1 0), and Cu(1 1 1), respectively). Data are presented in the form of atomic content ratio of Nb and Cu with respect to the total number of atoms in the simulated system. The vertical dashed lines mark the z coordinate of the Cu substrate surface prior to commencing the Nb and Ar particle deposition. The different line colors represent different deposition flux angles θ (panel(a); DCMS at $T = 450$ K) or different deposition temperatures T (panels (b)-(d); HiPIMS at $\theta = 0°$). Panel (e) shows depth profile of Cu, Nb, O, and C in a 150 nm thick Nb layer grown on Cu by HiPIMS as determined by XPS in combination with Ar^+ ion etching. The inset part shows the outermost surface on a magnified scale and the right graph the full distribution from the Nb surface towards the Nb/Cu interface with increasing sputter time. Panel (f) plots the cumulative fraction of sputtered Cu atoms f_{sp} (with respect to the initial number of Cu atoms in the simulation box) as a function of number of the deposited particles for HiPIMS growth simulations. Solid, dotted, and dashed lines correspond to data from simulations on Cu(1 0 0), Cu(1 1 0), and Cu(1 1 1) substrates, respectively. The different line colors correspond to data at different simulation temperatures, as indicated in the legend.

we observe that the segregation of Cu atoms at the film surface is more pronounced for Nb layers exhibiting an ⟨1 1 0⟩ out-of-plane crystallographic orientation, *i.e.*, for layers grown on Cu(1 0 0) and Cu(1 1 1).

The simulation data in Figs. 7(b) through (d) are complemented by XPS-measured depth compositional profiles of a 150 nm thick Nb layer grown by HiPIMS on Cu (Fig. 7(e)). Besides Nb, at the outermost surface C, O, and Cu are detected, the latter amounting ∼0.2 at.% (see inset in Fig. 7(e)). After 6 min of Ar^+ ion etching the Cu signal drops below the XPS detection limit and reemerges when ion etching approaches the Nb-Cu interface and the remaining Nb layer thickness is of the order of the inelastic mean free path of the photoelectrons. The presence of O and C at the surface is expected due to exposure of the sample to ambient during transport from the coating to the surface characterization apparatus. Moreover, the high reactivity of Nb that leads to the interaction with the residual gas in the UHV chamber is the reason why O and C content do not completely vanish when sputtering through the Nb film.

To better understand the processes of Cu diffusion and segregation evidenced from the HiPIMS growth simulations, we plot in Fig. 7(f)–for different simulation temperatures T–the cumulative fraction of sputtered Cu atoms f_{sp} (with respect to the initial number of Cu atoms in the simulation box) as a function of number of deposited atoms, for Cu(1 1 1) (dashed lines), Cu(1 0 0) (solid lines), and Cu(1 1 0) (dotted lines) surfaces. We see that for all deposition temperatures and substrate orientations f_{sp} initially increases. The initial linear loss of the atoms from the simulation box indicates ballistic sputtering of Cu atoms by energetic Nb ions, most notably at a temperature of 300 K where thermal evaporation is negligible. The latter becomes relevant at elevated temperatures, as evidenced by the increase of the linear slope when T increases from 300 K to 1000 K. We also see that the thicker the film grows the fewer atoms are sputtered away and the dependence f_{sp} on number of deposited atoms starts deviating from the linear function until it reaches saturation. The number of atoms at which the saturation is reached (see the black vertical arrows) shifts towards greater number of deposited atoms with an increase of temperature, *i.e.* from $\approx 1.1 \times 10^4$ at 300 K to $\approx 1.9 \times 10^4$ at 1000 K. Moreover, for all temperatures, the saturation value of f_{sp} displays a weak dependence on crystallographic orientation of the substrate surface, and increases from 8% at 300 K to 18% at 1000 K. These trends further support the notion that Nb-Cu intermixing and Cu evaporation during Nb condensation is governed by a complex interplay between thermally activated diffusion and ballistic-driven atomic rearrangement. Careful inspection of the data for $T = 1000$ K shows that, while f_{sp} values saturate above $\approx 2 \times 10^4$ atoms for simulations on Cu(1 1 1) and Cu(1 0 0) substrates, the curve for Cu(1 1 0) exhibits a small yet noticeable positive slope. This is consistent with the data in Fig. 7(c) which shows lesser presence of Cu near the interface of Cu(1 1 0)/Nb(2 0 0), than in two other cases (see Figs. 7(b) and (d)), which can be explained by easier migration of Cu atoms along the open [2 0 0] direction in Nb film than along the close-packed [1 1 0] direction.

3.3. Epitaxial relationships at the Nb-Cu interface

In Section 3.1, we see that our simulations predict that Nb films grow with different out-of-plane orientations on different Cu surfaces. In addition, depending on the simulation parameters, films may consist of either single or multiple grains. In the present section, we correlate these features with the epitaxial relationships between the Cu and Nb lattices at the film-substrate interface. We focus our discussion on data from HiPIMS deposition simulations which yield films of higher epitaxial quality, as compared to data from DCMS deposition simulations.

Fig. 8 presents top-view snapshots obtained from simulations of HiPIMS growth of Nb films on Cu after deposition of 25 000 Nb and 5 000 Ar atoms, whereby the size of the Nb and Cu atoms (green and pink spheres respectively) is reduced to better illustrate the orientation relationships between the film and the substrate lattices. The top row in Fig. 8 shows film-substrate systems in which the Nb film (simulation temperature $T = 300$ K) consists of a single grain on Cu(1 0 0)

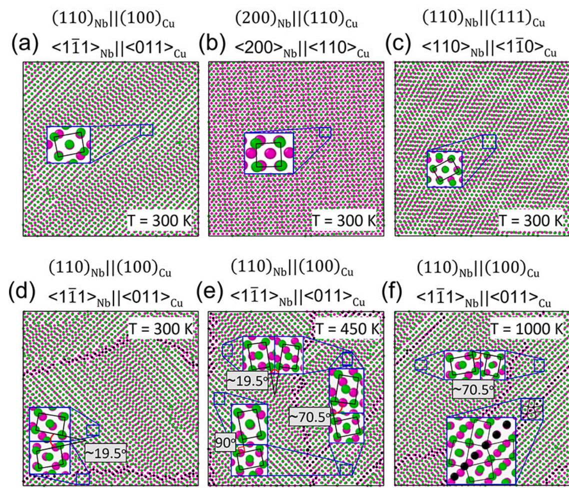

Fig. 8. Top-view snapshots of simulated atomic assemblies at parameters consistent with HiPIMS deposition of Nb films (25 000 Nb and 5 000 Ar atoms with energy 100 eV/atom) on Cu. The specific simulation parameters are (a) Cu(100) and $T = 300$ K; (b) Cu(110) and $T = 300$ K; (c) Cu(111) and $T = 300$ K; (d) Cu(100) and $T = 300$ K; (e) Cu(100) and $T = 450$ K; (f) Cu(100) and $T = 1000$ K. Panels (a) through (c) show snapshots from simulations in which only one crystalline domain is formed, while panels (d) through (f) show snapshots from simulations with multiple crystalline domains separated by domain boundaries. The size of Nb and Cu atoms (green and pink spheres respectively) is reduced to better illustrate the orientation relationships between the film and the substrate lattices, which is also highlighted via the magnified insets. The epitaxial relationship in the form of $(H\,K\,L)_{\mathrm{Nb}}||(h\,k\,l)_{\mathrm{Cu}};[U\,V\,W]_{\mathrm{Nb}}||[u\,v\,w]_{\mathrm{Cu}}$ is provided in each panel.

(panel (a)), Cu(1 1 0) panel ((b)), and Cu(1 1 1) (panel (c)). The insets in the figures are magnified views of the individual unit cells from the films and the substrate. From the insets, the following epitaxial orientation relationships are established for the various Cu surfaces: (i) $(1\,1\,0)_{\mathrm{Nb}}||(1\,1\,1)_{\mathrm{Cu}}$; $\langle 1\,1\,0\rangle_{\mathrm{Nb}}||\langle 1\,\bar{1}\,0\rangle_{\mathrm{Cu}}$, (ii) $(1\,1\,0)_{\mathrm{Nb}}||(1\,0\,0)_{\mathrm{Cu}}$; $\langle 1\,\bar{1}\,1\rangle_{\mathrm{Nb}}||\langle 0\,1\,1\rangle_{\mathrm{Cu}}$, and (iii) $(2\,0\,0)_{\mathrm{Nb}}||(1\,1\,0)_{\mathrm{Cu}}$;$\langle 2\,0\,0\rangle_{\mathrm{Nb}}||\langle 1\,1\,0\rangle_{\mathrm{Cu}}$, in agreement with the Nishiyama-Wasserman model based on the rigid lattice approximation [55], as well as experimental data for electron-beam evaporated and magnetron-sputtered Nb films on Cu substrates [56–59]. Besides the specific orientation relationships, all top-view snapshots in Figs. 8(a) through (c) exhibit Moiré patterns, most notably those corresponding to the Cu(1 1 1) and Cu(1 0 0) surfaces. This is because accommodation of the Nb lattice on the Cu(1 1 1) and Cu(1 0 0) requires that it rotates in-plane by 5.26° and 9.75°, respectively, along the [1 1 0] axis [60]. On the contrary, no rotation is necessary on Cu(1 1 0), but the lattice mismatch between Nb(2 0 0) and Cu(1 1 0) surfaces still produces a noticeable Moiré pattern.

The simulation data show that Nb films may consist of multiple grains, most frequently when growing on Cu(1 0 0). This is because the Nb(1 1 0)/Cu(1 0 0) overlayer is formed by four equivalent domains of Nb crystal grains (having the $[1\,\bar{1}\,1]$ direction parallel to the Cu[0 1 1] direction, with rotational symmetry of 90° [56]. For reference, the Nb(1 1 0)/Cu(1 1 1) overlayer is formed by three equivalent domains with rotational symmetry of 60°. Representative top-view snapshots of simulated multi-grain Nb films on Cu(1 0 0) at various temperatures are shown in Figs. 8(d) through (f). The grain boundaries mainly follow the lowest energy twin configuration with an angle between adjacent grains ∼ 19.5°, which is twice as large as the rotation angle between the Nb and Cu lattice of 9.75°. Some grains grow with a more complex grain boundary structure as crystal domains are rotated by ∼ 70.5° or ∼ 90° [56]. These configurations are observed at elevated temperatures since the grain boundaries of such a complex structure are associated with higher formation energy.

Besides the in-plane rotation of the film crystal lattice seen in Fig. 8, inspection of the simulation output shows that, for all parameters used in HiPIMS growth simulations, the film lattice planes are tilted with respect to the substrate normal. Typical data are shown in Figs. 9(a), (b), and (c) (HiPIMS simulations on Cu(1 0 0), Cu(1 1 0), and Cu(1 1 1), respectively; $T = 450$ and $\theta = 0°$) whereby the lattice tilt angle β ranges between 1.9° and 5.2°. We also note that data from simulations at different temperatures (not presented here) show that T has no systematic effect on the lattice tilt. In contrast to HiPIMS, no tilt is observed for simulation parameters consistent with DCMS deposition (see Figs. 9(d) through (f)). In the absence of misfit dislocations, tilt of lattice planes in epitaxial layers occurs when deposition occurs on vicinal surfaces and the out-of-plane lattice mismatch relaxes along the direction of the propagating steps [61]. In our model, low-index Cu surfaces are used as substrates, hence no vicinal surfaces exist in the starting configurations of our simulation boxes. However, as seen in Fig. 7, substantial intermixing occurs between Cu and Nb yielding a rough interface (Figs. 9(a)-(c)), that may provide atomic steps for strain relaxation to occur via lattice tilting. This is not the case for DCMS growth simulations (Figs. 9(d)-(f)) in which the interface is sharp and no intermixing is observed. Such lattice tilt has not been yet observed experimentally in earlier studies of Nb film growth on Cu using either thermalized [56] or low-energy vapor fluxes [57–59]. Hence, our data underscore the necessity for dedicated experimental studies of epitaxial orientation relationships and microstructure during growth of Nb on Cu by hyperthermal vapor fluxes.

4. Summary and conclusions

We present a combined computational and experimental study on the growth of Nb films, by DCMS and HiPIMS, on the complex-shaped curved surface of Cu rf cavities. Experimental data show that DCMS-grown films exhibit a columnar and seemingly dense morphology on the equatorial position of the cavity that faces directly the sputtering cathode and hence the Nb flux arrives at the substrate at near-to-normal incidence conditions. Films grown on the flat slope of the cavity at the iris position (oblique-angle deposition conditions) are still columnar, but the columns are tilted towards the direction of the deposition flux and the microstructure is porous. In contrast to DCMS, HiPIMS-grown films exhibit a dense microstructure with columns growing perpendicularly to the substrate surface, irrespective of the area of deposition.

Classical Molecular Dynamics simulations are used to model Nb growth at conditions consistent with DCMS and HiPIMS deposition. Our simulation data reproduce the overall trends with respect to film morphology and microstructure established at the various experimental conditions. Moreover, analysis of the evolution of the simulated systems allows us to conclude that the dense microstructure of the HiPIMS-grown layers (as compared to their DCMS counterparts) emerges as result of (i) deflection of ionized sputtered species to a direction parallel to the substrate normal by the electric field between the plasma and the bias potential and (ii) bombardment-induced interruption of local epitaxial (*i.e.*, crystal) growth through all film formation stages. Besides the atomic-scale mechanisms that control growth evolution, the simulations predict that HiPIMS growth atomic intermixing at the film-substrate interface due to ballistic- and thermally-induced effects. This intermixing results in incorporation of Cu in the Nb film bulk close to the film-substrate interface, as well as Cu segregation on the Nb film surface. The incorporation of Cu in the vicinity of the interface is seemingly correlated with tilt of the Nb lattice planes relative to the Cu substrate lattice planes, the latter being a phenomenon that has not been observed in experimental studies of Nb on Cu using thermalized on low-energy vapor fluxes. Moreover, experimental data confirm the presence of Cu on the Nb film surface, which may affect the performance of the rf cavity. The overall conclusion of our study is that knowledge-based design of plasma coating processes for the Nb-Cu system for the next generation of rf cavities can be supported by strategically combining atomistic simulation with characterization tools capable of providing structural and compositional information at the nanoscale.

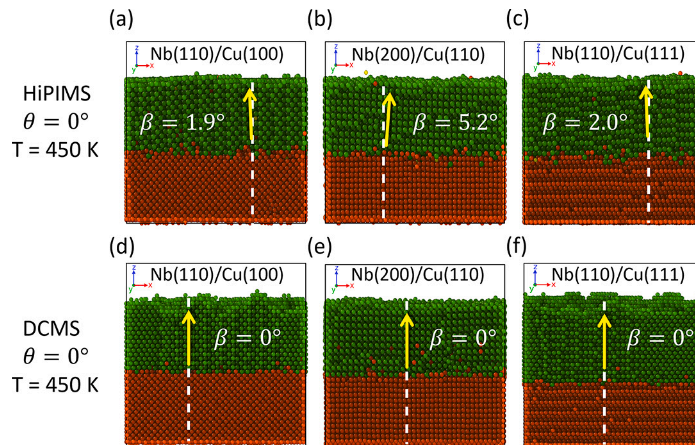

Fig. 9. Cross-sectional snapshots of atomic assemblies (Nb and Cu are represented by green and red spheres, respectively) generated by simulating growth of Nb at $T = 450$ K and $\theta = 0°$ at conditions resembling HiPIMS on (a) Cu(1 0 0), (b) Cu(1 1 0), (c) Cu(1 1 1) and DCMS on (d) Cu(1 0 0), (e) Cu(1 1 0), (f) Cu(1 1 1). The vertical dashed lines show the direction of the Cu substrate lattice as normal while the arrows mark the direction of the film lattice as normal. The tilt angle β between the substrate and the film lattice normal is provided in each panel.

CRediT authorship contribution statement

M. Ghaemi: Conceptualization, Formal analysis, Methodology, Software, Validation, Visualization, Writing – original draft. **A. Lopez-Cazalilla:** Conceptualization, Supervision, Writing – original draft. **K. Sarakinos:** Conceptualization, Supervision, Writing – review & editing. **G.J. Rosaz:** Investigation, Resources. **C.P.A. Carlos:** Investigation, Resources. **S. Leith:** Investigation, Resources. **S. Calatroni:** Investigation, Resources. **M. Himmerlich:** Investigation, Resources. **F. Djurabekova:** Conceptualization, Supervision, Writing – review & editing.

Declaration of competing interest

The authors declare that they have no known competing financial interests or personal relationships that could have appeared to influence the work reported in this paper.

Data availability

Data will be made available on request.

Acknowledgements

Computer time granted by the IT Center for Science – CSC – Finland and the Finnish Grid and Cloud Infrastructure (persistent identifier urn:nbn:fi:research-infras-2016072533) is gratefully acknowledged. KS acknowledges financial support from the Swedish Research Council (Grant No. VR-2021-04113) and the Åforsk foundation (Grant No. 22-150).

Appendix A. Supplementary material

Supplementary material related to this article can be found online at https://doi.org/10.1016/j.surfcoat.2023.130199.

References

[1] Patrick Marchand, Superconducting rf cavities for synchrotron light sources, in: Proceedings of EPAC'04, 2004, p. 21.
[2] A. Miyazaki, W. Venturini Delsolaro, Two different origins of the q-slope problem in superconducting niobium film cavities for a heavy ion accelerator at cern, Phys. Rev. Accel. Beams 22 (2019) 073101.
[3] Walter Venturini Delsolaro, Eric Montesinos, Mathieu Therasse, Yacine Kadi, Lloyd Williams, Ofelia Capatina, Guillaume Rosaz, Silvia Teixeira Lopez, Alban Sublet, Karl-Martin Schirm, et al., Jacow: lessons learned from the HIE-Isolde cavity production and cryomodule commissioning, https://doi.org/10.18429/JACoW-SRF2017-TUXAA02, 2018.
[4] V. Arbet-Engels, Cristoforo Benvenuti, S. Calatroni, Pierre Darriulat, M.A. Peck, A-M. Valente, C.A. Van't Hof, Superconducting niobium cavities, a case for the film technology, Nucl. Instrum. Methods Phys. Res., Sect. A, Accel. Spectrom. Detect. Assoc. Equip. 463 (2001) 1–8.
[5] Cristoforo Benvenuti, N. Circelli, M. Hauer, Niobium films for superconducting accelerating cavities, Appl. Phys. Lett. 45 (1984) 583–584.
[6] Daniel Boussard, E. Chiaveri, E. Haebel, H.P. Kindermann, R. Losito, S. Marque, V. Rodel, M. Stirbet, The lhc superconducting cavities, in: Proceedings of the 1999 Particle Accelerator Conference (Cat. No. 99CH36366), vol. 2, IEEE, 1999, pp. 946–948.
[7] L. Lain Amador, P. Chiggiato, L.M.A. Ferreira, E. Garcia-Tabares, T. Koettig, M.S. Meyer, A.T. Perez-Fontenla, K. Puthran, G. Rosaz, M. Taborelli, Electrodeposition of copper applied to the manufacture of seamless superconducting rf cavities, Phys. Rev. Accel. Beams 24 (2021) 082002.
[8] Gianluigi Ciovati, Effect of low-temperature baking on the radio-frequency properties of niobium superconducting cavities for particle accelerators, J. Appl. Phys. 96 (2004) 1591–1600.
[9] Marco Arzeo, F. Avino, S. Pfeiffer, G. Rosaz, M. Taborelli, L. Vega-Cid, W. Venturini-Delsolaro, Enhanced radio-frequency performance of niobium films on copper substrates deposited by high power impulse magnetron sputtering, Supercond. Sci. Technol. 35 (2022) 054008.
[10] E. Bemporad, F. Carassiti, M. Sebastiani, G. Lanza, V. Palmieri, H. Padamsee, Superconducting and microstructural studies on sputtered niobium thin films for accelerating cavity applications, Supercond. Sci. Technol. 21 (2008) 125026.
[11] G. Terenziani, S. Calatroni, A.P. Ehiasarian, "Nb coatings for superconducting rf applications by hipims", Private Communication, in: CERN, 2013.
[12] Guillaume Rosaz, Aleksandra Bartkowska, Carlota P.A. Carlos, Thibaut Richard, Mauro Taborelli, Niobium thin film thickness profile tailoring on complex shape substrates using unbalanced biased high power impulse magnetron sputtering, Surf. Coat. Technol. 436 (2022) 128306.
[13] Chapter 1 - deposition technologies: an overview, in: Handbook of Deposition Technologies for Films and Coatings, third edition, 2010, pp. 1–31.
[14] Milton Ohring, Chapter 4 - discharges, plasmas, and ion–surface interactions, in: Materials Science of Thin Films, second edition, 2002, pp. 145–202.
[15] S. Mahieu, P. Ghekiere, D. Depla, R. De Gryse, Biaxial alignment in sputter deposited thin films, Thin Solid Films 515 (2006) 1229–1249.
[16] Jones Alami, P.O.Å. Persson, Denis Music, J-T. Gudmundsson, J. Bohlmark, Ulf Helmersson, Ion-assisted physical vapor deposition for enhanced film properties on nonflat surfaces, J. Vac. Sci. Technol., A, Vac. Surf. Films 23 (2005) 278–280.
[17] K. Bobzin, N. Bagcivan, P. Immich, S. Bolz, J. Alami, R. Cremer, Advantages of nanocomposite coatings deposited by high power pulse magnetron sputtering technology, J. Mater. Process. Technol. 209 (2009) 165–170.
[18] G. Greczynski, J. Jensen, L. Hultman, Mitigating the geometrical limitations of conventional sputtering by controlling the ion-to-neutral ratio during high power pulsed magnetron sputtering, Thin Solid Films 519 (2011) 6354–6361.
[19] Viktor Elofsson, Daniel Magnfält, M. Samuelsson, Kostas Sarakinos, Tilt of the columnar microstructure in off-normally deposited thin films using highly ionized vapor fluxes, J. Appl. Phys. 113 (2013) 174906.
[20] Kostas Sarakinos, Jones Alami, Stephanos Konstantinidis, High power pulsed magnetron sputtering: a review on scientific and engineering state of the art, Surf. Coat. Technol. 204 (2010) 1661–1684.
[21] Reza Namakian, Brian R. Novak, Xiaoman Zhang, Wen Jin Meng, Dorel Moldovan, A combined molecular dynamics/Monte Carlo simulation of cu thin film growth on tin substrates: illustration of growth mechanisms and comparison with experiments, Appl. Surf. Sci. 570 (2021) 151013.

[22] Annemie Bogaerts, Evi Bultinck, Ivan Kolev, Laurent Schwaederlé, Koen Van Aeken, Guy Buyle, Diederik Depla, Computer modelling of magnetron discharges, J. Phys. D, Appl. Phys. 42 (2009) 194018.
[23] Movaffaq Kateb, Hamidreza Hajihoseini, Jon-Tomas Gudmundsson, Snorri Ingvarsson, Role of ionization fraction on the surface roughness, density, and interface mixing of the films deposited by thermal evaporation, dc magnetron sputtering, and hipims: an atomistic simulation, J. Vac. Sci. Technol. A 37 (2019) 031306, https://doi.org/10.1116/1.5094429.
[24] Daniel Lundin, Tiberiu Minea, Jon Tomas Gudmundsson, High Power Impulse Magnetron Sputtering: Fundamentals, Technologies, Challenges and Applications, Elsevier, 2019.
[25] Guillaume Rosaz, Aleksandra Bartkowska, Carlota P.A. Carlos, Thibaut Richard, Mauro Taborelli, Niobium thin film thickness profile tailoring on complex shape substrates using unbalanced biased high power impulse magnetron sputtering, Surf. Coat. Technol. 436 (2022) 128306.
[26] CERN, Presentazione Cern on HiPIMS results, https://indico.cern.ch/event/181352/contributions/1451039/attachments/244012/341426/Presentazione_Cern_on_HiPIMS_results.pdf. (Accessed 11 July 2022).
[27] A. Lopez-Cazalilla, et al., Modeling of high-fluence irradiation of amorphous Si and crystalline Al by linearly focused Ar ions, J. Phys. Condens. Matter 31 (2018) 075302.
[28] A. Lopez-Cazalilla, et al., Direct observation of ion-induced self-organization and ripple propagation processes in atomistic simulations, Mater. Res. Lett. 8 (2020) 110–116.
[29] S. Plimpton, Fast parallel algorithms for short-range molecular dynamics, J. Comput. Phys. 117 (1995) 1–19.
[30] Yu Mishin, M.J. Mehl, D.A. Papaconstantopoulos, A.F. Voter, J.D. Kress, Structural stability and lattice defects in copper: ab initio, tight-binding, and embedded-atom calculations, Phys. Rev. B 63 (2001) 224106.
[31] G.J. Ackland, R. Thetford, An improved n-body semi-empirical model for body-centred cubic transition metals, Philos. Mag. A 56 (1987) 15–30.
[32] Liang Zhang, Martinez Enrique, Caro Alfredo, Liu Xiang-Yang, Michael J. Demkowicz, Liquid-phase thermodynamics and structures in the cu–nb binary system, Model. Simul. Mater. Sci. Eng. 21 (2013) 025005.
[33] H. Okamoto, Cu-Nb (copper-niobium), J. Phase Equilib. 12 (1991) 614–615.
[34] Shujing Dong, Tianju Chen, Sixie Huang, Nan Li, Caizhi Zhou, Thickness-dependent shear localization in cu/nb metallic nanolayered composites, Scr. Mater. 187 (2020) 323–328.
[35] K. Nordlund, et al., Repulsive interatomic potentials calculated using Hartree-Fock and density-functional theory methods, Nucl. Instrum. Methods Phys. Res. B 132 (1997) 45–54.
[36] Joachim Burgdorfer, Fred Meyer, Above-surface neutralization of highly charged ions: the formation of hollow atoms, Phys. Scr. T 46 (1993) 225.
[37] Alexander Stukowski, Visualization and analysis of atomistic simulation data with ovito–the open visualization tool, Model. Simul. Mater. Sci. Eng. 18 (2009) 015012.
[38] Alexander Stukowski, Computational analysis methods in atomistic modeling of crystals, JOM 66 (2014) 399–407.
[39] J. Hrn Scofield, Hartree-slater subshell photoionization cross-sections at 1254 and 1487 ev, J. Electron Spectrosc. Relat. Phenom. 8 (1976) 129–137.
[40] A. Jablonski, Universal energy dependence of the inelastic mean free path, Surf. Interface Anal. 20 (1993) 317–321.
[41] J.E. Greene, Chapter 12 - thin film nucleation, growth, and microstructural evolution: an atomic scale view, in: Handbook of Deposition Technologies for Films and Coatings, third edition, 2010, pp. 554–620.
[42] I. Petrov, P.B. Barna, Lars Hultman, J.E. Greene, Microstructural evolution during film growth, J. Vac. Sci. Technol., A, Vac. Surf. Films 21 (2003) S117–S128.
[43] P.B. Barna, M. Adamik, Fundamental structure forming phenomena of polycrystalline films and the structure zone models, Thin Solid Films 317 (1998) 27–33.
[44] Michael T. Taschuk, Matthew M. Hawkeye, Michael J. Brett, Chapter 13 - glancing angle deposition, in: Handbook of Deposition Technologies for Films and Coatings, third edition, 2010, pp. 621–678.
[45] J. Hopwood, Ionized physical vapor deposition of integrated circuit interconnects, Phys. Plasmas 5 (1998) 1624–1631.
[46] M.V. Ramana Murty, Harry A. Atwater, A.J. Kellock, J.E.E. Baglin, Very low temperature ($<400^{\circ}$ c) silicon molecular beam epitaxy: the role of low energy ion irradiation, Appl. Phys. Lett. 62 (1993) 2566–2568.
[47] The Physical Properties of Thin Ag Films Formed Under the Simultaneous Ion Implantation in the Substrate, Nucl. Instrum. Methods Phys. Res. 209–210 (1983) 179–184.
[48] Effect of Ion Bombardment on the Initial Stages of Thin Film Growth, Thin Solid Films 46 (1977) 267–274.
[49] E. Chason, P. Bedrossian, K.M. Horn, J.Y. Tsao, S.T. Picraux, Ion beam enhanced epitaxial growth of ge (001), Appl. Phys. Lett. 57 (1990) 1793–1795.
[50] The Nucleation and Initial Growth of Gold Films Deposited onto Sodium Chloride by Ion-Beam Sputtering, Thin Solid Films 26 (1975) 5–23.
[51] Thomas Michely, George Comsa, The scanning tunneling microscope as a means for the investigation of ion bombardment effects on metal surfaces, Nucl. Instrum. Methods Phys. Res., Sect. B, Beam Interact. Mater. Atoms 82 (1993) 207–219.
[52] Georg Rosenfeld, Roland Servaty, Christian Teichert, Bene Poelsema, George Comsa, Layer-by-layer growth of ag on ag (111) induced by enhanced nucleation: a model study for surfactant-mediated growth, Phys. Rev. Lett. 71 (1993) 895.
[53] G. Rosenfeld, N.N. Lipkin, W. Wulfhekel, J. Kliewer, K. Morgenstern, B. Poelsema, G. Comsa, New concepts for controlled homoepitaxy, Appl. Phys. A 61 (1995) 455–466.
[54] J. Alami, Kostas Sarakinos, F. Uslu, M. Wuttig, On the relationship between the peak target current and the morphology of chromium nitride thin films deposited by reactive high power pulsed magnetron sputtering, J. Phys. D, Appl. Phys. 42 (2008) 015304.
[55] Z. Nishiyama, Sci. Rept. Tohoku Univ. 23 (1934) 325.
[56] K. Masek, V. Matolin, Rheed study of nb thin film growth on cu(111) and (100) single-crystals, in: Proceedings of the 8th Joint Vaccum Conference of Croatia, Austria, Slovenia and Hungary, in: Vacuum, vol. 61, 2001, pp. 217–221.
[57] Terence E. Mitchell, Yong Cheng Lu, Alfred J. Griffin Jr., Michael Nastasi, Harriet Kung, Structure and mechanical properties of copper/niobium multilayers, J. Am. Ceram. Soc. 80 (1997) 1673–1676.
[58] Nathan A. Mara, Irene J. Beyerlein, Effect of bimetal interface structure on the mechanical behavior of cu–nb fcc–bcc nanolayered composites, J. Mater. Sci. 49 (2014) 6497–6516.
[59] A. Misra, R.G. Hoagland, H. Kung, Thermal stability of self-supported nanolayered cu/nb films, Philos. Mag. 84 (2004) 1021–1028.
[60] O. Hellwig, K. Theis-Bröhl, G. Wilhelmi, A. Stierle, H. Zabel, Growth of fcc (111) on bcc (110): new type of epitaxial transition observed for pd on cr, Surf. Sci. 398 (1998) 379–385.
[61] J.E. Ayers, S.K. Ghandhi, L.J. Schowalter, Crystallographic tilting of heteroepitaxial layers, J. Cryst. Growth 113 (1991) 430–440.